ARTICLES
https://doi.org/10.1038/s41561-020-0534-0

nature geoscience

Check for updates

The atmosphere of Mars as observed by InSight

Don Banfield[1,29]✉, Aymeric Spiga[2,3,29]✉, Claire Newman[4], François Forget[2], Mark Lemmon[5], Ralph Lorenz[6], Naomi Murdoch[7], Daniel Viudez-Moreiras[8], Jorge Pla-Garcia[5,8], Raphaël F. Garcia[7], Philippe Lognonné[3,9], Özgür Karatekin[10], Clément Perrin[9], Léo Martire[7], Nicholas Teanby[11], Bart Van Hove[10], Justin N. Maki[12], Balthasar Kenda[9], Nils T. Mueller[13], Sébastien Rodriguez[3,9], Taichi Kawamura[9], John B. McClean[14], Alexander E. Stott[14], Constantinos Charalambous[14], Ehouarn Millour[2], Catherine L. Johnson[15,16], Anna Mittelholz[15], Anni Määttänen[17], Stephen R. Lewis[18], John Clinton[19], Simon C. Stähler[20], Savas Ceylan[20], Domenico Giardini[20], Tristram Warren[21], William T. Pike[14], Ingrid Daubar[22], Matthew Golombek[12], Lucie Rolland[23], Rudolf Widmer-Schnidrig[24], David Mimoun[7], Éric Beucler[25], Alice Jacob[9], Antoine Lucas[9], Mariah Baker[26,27], Véronique Ansan[25], Kenneth Hurst[12], Luis Mora-Sotomayor[8], Sara Navarro[8], Josefina Torres[8], Alain Lepinette[8], Antonio Molina[8], Mercedes Marin-Jimenez[8], Javier Gomez-Elvira[8], Veronica Peinado[8], Jose-Antonio Rodriguez-Manfredi[8], Brian T. Carcich[1], Stephen Sackett[1], Christopher T. Russell[28], Tilman Spohn[13], Suzanne E. Smrekar[12] and W. Bruce Banerdt[12]

The atmosphere of Mars is thin, although rich in dust aerosols, and covers a dry surface. As such, Mars provides an opportunity to expand our knowledge of atmospheres beyond that attainable from the atmosphere of the Earth. The InSight (Interior Exploration using Seismic Investigations, Geodesy and Heat Transport) lander is measuring Mars's atmosphere with unprecedented continuity, accuracy and sampling frequency. Here we show that InSight unveils new atmospheric phenomena at Mars, especially in the higher-frequency range, and extends our understanding of Mars's meteorology at all scales. InSight is uniquely sensitive to large-scale and regional weather and obtained detailed in situ coverage of a regional dust storm on Mars. Images have enabled high-altitude wind speeds to be measured and revealed airglow—faint emissions produced by photochemical reactions—in the middle atmosphere. InSight observations show a paradox of aeolian science on Mars: despite having the largest recorded Martian vortex activity and dust-devil tracks close to the lander, no visible dust devils have been seen. Meteorological measurements have produced a catalogue of atmospheric gravity waves, which included bores (soliton-like waves). From these measurements, we have discovered Martian infrasound and unexpected similarities between atmospheric turbulence on Earth and Mars. We suggest that the observations of Mars's atmosphere by InSight will be key for prediction capabilities and future exploration.

The atmosphere of Mars has an average pressure that is 0.6% of Earth's. It lacks moist convection, but responds strongly to airborne dust heating. Mars's unique atmospheric regime offers the opportunity to study meteorological phenomena from planetary scales (thermal tides, baroclinic instability and dust storms) to regional scales (slope winds and gravity waves) and local scales (turbulence), all of which are expected to be stronger than those on Earth[1]. Mars also has unearthly characteristics, such as the main

[1]Cornell University, Cornell Center for Astrophysics and Planetary Science, Ithaca, NY, USA. [2]Laboratoire de Météorologie Dynamique/Institut Pierre Simon Laplace (LMD/IPSL), Sorbonne Université, Centre National de la Recherche Scientifique (CNRS), École Polytechnique, École Normale Supérieure (ENS), Paris, France. [3]Institut Universitaire de France, Paris, France. [4]Aeolis Research, Chandler, AZ, USA. [5]Space Science Institute, Boulder, CO, USA. [6]Johns Hopkins Applied Physics Laboratory, Laurel, MD, USA. [7]Institut Supérieur de l'Aéronautique et de l'Espace (ISAE-SUPAERO), Toulouse, France. [8]Centro de Astrobiología (INTA-CSIC), Madrid, Spain. [9]Université de Paris, Institut de Physique du Globe de Paris, CNRS, Paris, France. [10]Royal Observatory of Belgium, Directorate 'Reference Systems and Planetology', Brussels, Belgium. [11]School of Earth Sciences, University of Bristol, Bristol, UK. [12]Jet Propulsion Laboratory, California Institute of Technology, Pasadena, CA, USA. [13]German Aerospace Center (DLR), Institute of Planetary Research, Berlin, Germany. [14]Department of Electrical and Electronic Engineering, Imperial College London, London, UK. [15]Department of Earth, Ocean and Atmospheric Sciences, University of British Columbia, Vancouver, British Columbia, Canada. [16]Planetary Science Institute, Tucson, AZ, USA. [17]Laboratoire Atmosphère Milieux Observations Spatiales/Institut Pierre-Simon Laplace (LATMOS/IPSL), Sorbonne Université, Université Paris-Saclay, Université de Versailles Saint-Quentin-en-Yvelines, Centre National de la Recherche Scientifique, Guyancourt, France. [18]School of Physical Sciences, The Open University, Milton Keynes, UK. [19]Swiss Seismological Service (SED), ETH Zurich, Zurich, Switzerland. [20]Institute of Geophysics, ETH Zurich, Zurich, Switzerland. [21]Department of Physics, University of Oxford, Oxford, UK. [22]Department of Earth, Environmental, and Planetary Sciences, Brown University, Providence, RI, USA. [23]Université Côte d'Azur, Observatoire de la Côte d'Azur, CNRS, IRD, Géoazur, Valbonne, France. [24]Black Forest Observatory, Stuttgart University, Wolfach, Germany. [25]Laboratoire de Planétologie et Géodynamique, UMR6112, Université Nantes, Université Angers, CNRS, Nantes, France. [26]Morton K. Blaustein Department of Earth and Planetary Sciences, Johns Hopkins University, Baltimore, MD, USA. [27]Center for Earth and Planetary Studies, National Air and Space Museum, Smithsonian Institution, Washington DC, USA. [28]Department of Earth, Planetary, and Space Sciences, University of California, Los Angeles, CA, USA. [29]These authors contributed equally to this work: Don Banfield, Aymeric Spiga. ✉e-mail: banfield@astro.cornell.edu; aymeric.spiga@sorbonne-universite.fr

atmospheric component, carbon dioxide (CO_2), condensing on the Martian polar regions[2] and in the middle atmosphere[3].

Outstanding questions about Mars's atmosphere remain open. What is the subtle balance of phenomena that accounts for the atmospheric variability at a given location on Mars? How is dust lifted from the surface? How can we use Mars as a laboratory to explore key meteorological phenomena on Earth? To address those questions, in situ temporal coverage at Mars's surface is crucial to provide ground truth for Martian atmospheric models and to supplement orbital observations, which at a given location on Mars provide infrequent coverage and sense mostly in the middle-to-upper atmosphere. Previous lander missions conducted atmospheric measurements at the surface of Mars[4,5], yet no continuous measurements by a high-sensitivity meteorological station able to monitor atmospheric processes across a range of scales, from large-scale weather to small-scale turbulence, have been performed.

After successful entry, descent and landing (EDL; reconstructed temperature profile in Fig. 1a), the InSight mission landed at 4.5° N 135.6° E in Elysium Planitia on Mars in the northern winter (Extended Data Figs. 1 and 2). The first 200 Martian solar days (sol, 1 sol = 88,775 s) of atmospheric measurements demonstrate how InSight can both unveil atmospheric phenomena not measured at the surface of Mars and explore known phenomena with a fresh perspective. The InSight lander is the first continuously operating weather station at the surface of Mars (Figs. 1b and 2) and the first to feature a high-frequency high-precision pressure sensor[6,7] (Methods). Moreover, InSight's wind measurement capabilities, with two operating medium-frequency wind sensors, are only matched by those of the Viking landers; quantitative wind measurements on board all the other previous missions[4] were either lacking[8], at a low sampling frequency[9] or made difficult by damage during landing on Mars[10]. New perspectives for atmospheric science are also opened by using the wind- and pressure-induced 'noise' in the signal acquired by the InSight SEIS (Seismic Experiment for Interior Structure) seismometers[7,11,12].

Large-scale atmospheric phenomena

Mars has daily weather variations, as evidenced from landers[9,13] and orbiters[14], that result from mid-latitude planetary waves caused by baroclinic instability related to seasonal equator-to-pole temperature gradients. Contrary to that of Earth, the behaviour of the Martian atmosphere in the mid-latitudes is simply governed by alternating dominant baroclinic modes, for reasons still unclear[15]. Surprisingly, InSight's high-sensitivity tropical pressure measurements are a valuable reference to study baroclinic instability in the mid-latitudes. When seasonal and diurnal trends are removed from InSight's pressure and wind measurements (Fig. 3), a clear wave pattern of a 2.5 sol period is detected in the first 40 sols of the mission, which corresponds to the peak amplitude of northern winter's mid-latitude transient waves[16], which later changes to a 5–6 sol period at the end of northern winter and a 4 sol period in northern spring (Extended Data Fig. 3). Baroclinic waves at equatorial latitudes were previously detected using Curiosity data[17], but in comparison the InSight measurements, with improved sensitivity and continuity, are remarkably clear and regular.

In Mars's thin, sunlight-controlled atmosphere, weather is impacted by airborne dust. InSight is the first wind-measuring weather station since the Viking landers 40 years ago[18] to experience the impact of a regional-scale dust storm. The storm started on the other side of Mars[19] before spreading dust around the planet and doubling the atmospheric dust optical depth at InSight between sols 40 and 50 (Fig. 1c). Consequently, and as expected from theory[1], the diurnally repeating pressure variation increased as both the diurnal and semidiurnal tidal components amplified. In addition, the diurnal cycle of wind direction changed from a small angular fluctuation to a complete anticlockwise rotation over a sol (Fig. 2d). During this regional dust storm, the synoptic variability in pressure and wind (Fig. 3a,b) was deeply impacted and transitioned from a well-identified 2.5 sol mode to longer-period modes (7–10-sol periods; Fig. 3 and Extended Data Fig. 3b). This transition is thought to act as a negative feedback for the development of dust storms on Mars[20,21].

InSight's ability to monitor meteorological phenomena at larger horizontal scales than its immediate surroundings also includes the vertical dimension for middle-atmosphere processes through colour-imaging capabilities. InSight's cameras, operating just after sunset, observed noctilucent clouds[3,8] at the transition between northern winter and spring (Fig. 1d). Given the position of the Sun, these clouds must have been at least 50 km above the surface to be illuminated. Past orbital detection of mesospheric clouds at this altitude and season suggests either water–ice or CO_2–ice clouds[22,23]. Cloud motions indicate east-southeasterly wind speeds of 40–60 m s^{-1} assuming a 60 km altitude—an altitude at which wind speed has seldom been evaluated on Mars[24,25]. Furthermore, night-time imaging showed that sky brightness persisted long after twilight, not attributable to moonlight. The relative contributions in the Instrument Deployment Camera (IDC) colour filters are consistent with a 577.8 nm airglow of order 10 Rayleighs. This airglow, produced by photochemical reactions in the upper atmosphere, was expected but not previously confirmed on Mars[26].

Diurnal and subdiurnal variability

Mars, with its uniquely low average surface pressure, highlights an end-member case of sunlight control of the diurnal cycle, particularly as compared to Earth. This causes on Mars (relative to Earth): (1) atmospheric thermal tides an order of magnitude stronger,[27], especially in low-latitudes; (2) more sustained daytime upslope and night-time downslope flows[28], especially over steep slopes[29] and (3) a much sharper contrast between the strong daytime, buoyancy-driven convective turbulence and the moderate night-time, shear-driven mechanical turbulence[30].

InSight's atmospheric measurements allow this picture, drawn from existing observations, to be refined. Consistent with previous measurements[2,31] and modelling[7,32], InSight has recorded a diurnally repeating cycle of pressure (Fig. 2a) that shows the major impact of diurnal and semidiurnal thermal tides on the Martian atmosphere. This makes thermal tides the best candidate to explain the large diurnal deviation in wind direction, recorded by InSight's wind sensors (Fig. 2d) and consistently inferred by SEIS seismometers from wind-induced perturbations. Nevertheless, despite the fact that InSight landed on a nearly flat plain, the diurnal cycle of wind direction measured by InSight appears to be due primarily to flows induced by the nearby gentle regional slope rather than by thermal tides. Afternoon winds are upslope (from the northeast) and night-time winds are downslope (from the southwest), except when the prevailing large-scale winds from the northwest are strong enough to dominate (Fig. 2d). Although global climate modelling using realistic topography reproduces these diurnal winds, artificially flattening the local plains around InSight in the model causes them to disappear (Extended Data Fig. 4).

Gravity waves, which have buoyancy as their restoring force, are the dominant process that governs the variability in planetary atmospheres at regional spatial scales and at timescales of several hundreds of seconds[33]; their propagation and breaking also impacts large-scale wind and temperature in the upper atmosphere[34]. Both gravity-wave oscillations, with vertical wavelengths of a couple kilometres[35], and dry adiabatic layers at mesospheric altitudes of 60–70 km, which denote gravity-wave breaking and subsequent heat mixing, are detectable in the temperature profile acquired during InSight's entry, descent and landing (Fig. 1a). On the detection of gravity waves, the continuous fine-sensitivity coverage by InSight's pressure sensor fills a gap left by previous studies—orbital

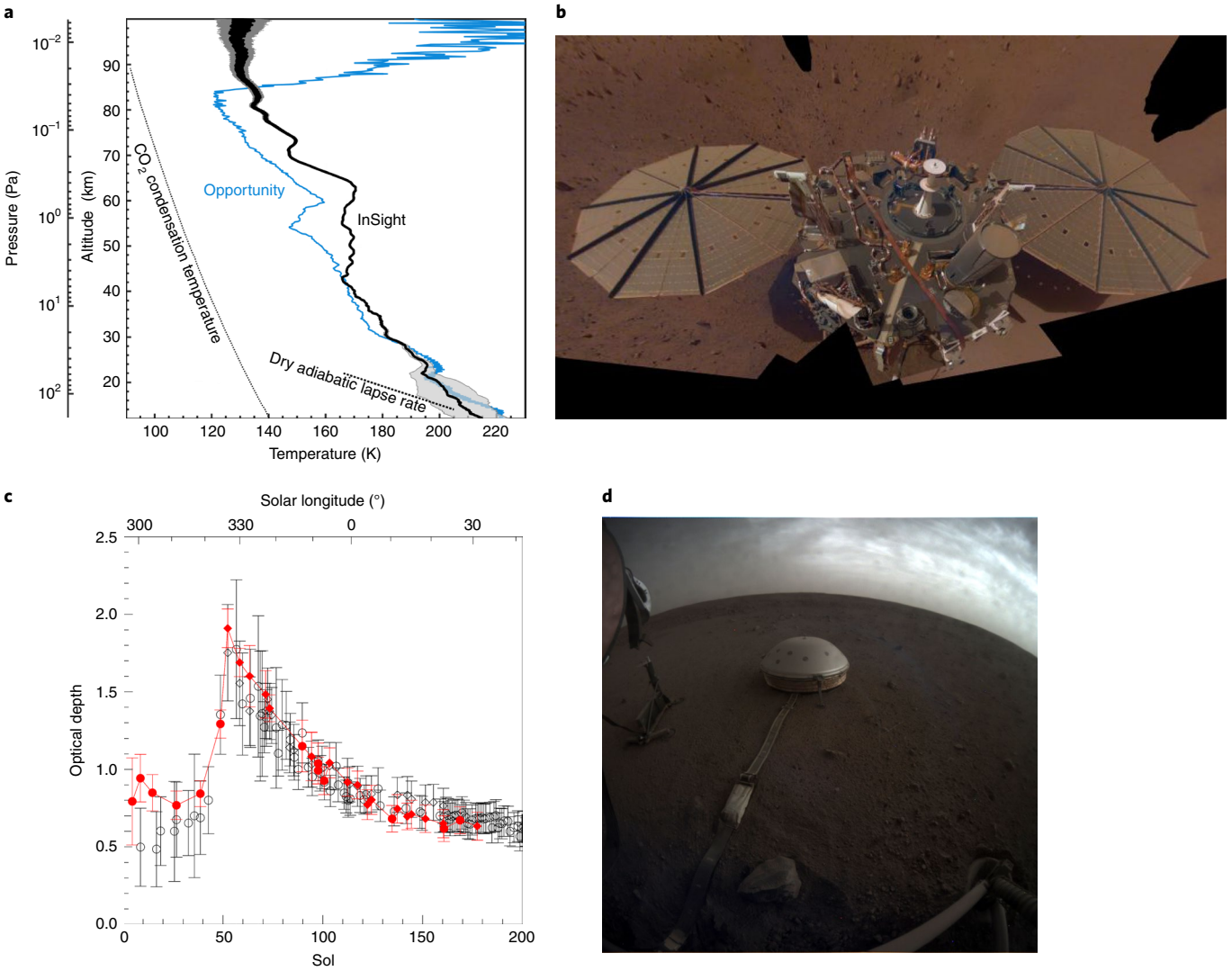

Fig. 1 | After successful EDL, InSight now provides continuous weather data for Mars. a, Reconstructed temperature profile (with 3σ error bars) from InSight's EDL; the profile obtained for Opportunity at a similar location and season[64], the CO_2 condensation profile and a dry adiabatic lapse rate are included for reference. **b**, Mosaic of InSight's deck imaged on sols 106 and 133 (solar longitude (L_s) = 356° and 10°, respectively) that features the two Temperature and Wind for InSight (TWINS) booms facing outward, which overlook the dusty solar panels, and the pressure sensor's inlet in the middle (Image PIA23203). **c**, Atmospheric dust optical depth obtained from IDC (red) and ICC (black) imaging in the morning (diamonds) and evening (circles); 1σ error bars, dominated by the systematic effects in the tau retrieval, are indicated on the plot. **d**, ICC image on sol 145 (L_s = 16°) showing noctilucent clouds after sunset, with the HP^3 (Heat Flow and Physical Properties Package) suite, and the SEIS below the wind and thermal shield in the foreground (Image PIA23180).

observations can only provide infrequent coverage at a given location[36,37] and in situ observations are limited to the specific setting of Curiosity[5,38] within the Gale Crater whose nearby rims are the likely wave source[39]. Located in the flat plains of Elysium Planitia, the InSight pressure measurements exhibit numerous examples of 300–800 s gravity-wave pressure fluctuations from early evening to late at night (Fig. 4a), sometimes reaching 2 Pa peak-to-peak. Furthermore, in rare instances in the middle of the night, InSight captured yet undetected simultaneous and coherent gravity-wave fluctuations of pressure and wind with long periods of ~1,500 s and estimated horizontal wavelengths of ~25–35 km and phase speeds of ~15–25 m s^{-1} (Methods and Extended Data Figs. 5 and 6). InSight demonstrates convincingly that the gravity-wave activity (1) systematically peaks in the evening and early night, (2) appears absent in daytime (3) is highly variable from one sol to another and (4) undergoes significant seasonal variability; for instance, two successive wave trains often detected each sol from sol 120 to 150 are followed by almost no detected waves from sol 150 to 200. The intense gravity-wave activity at the InSight landing site, far from any topographical obstacles, indicates that waves either originate from strong winds that interact with sharp topographic features at particularly large distances or that non-orographic sources (for example, jet acceleration and convection) are involved.

In the decaying phase of the sol 40 regional dust storm, InSight detected a signal reminiscent of terrestrial atmospheric bores and solitary waves (Fig. 4b), caused on Earth by the propagation of a cold front that leads to, for example, 'Morning Glory' clouds[40]. For Mars, modelling studies proposed bores as an explanation for enigmatic elongated clouds[41] and the hydraulic-jump analogues of low-latitude bores as instrumental for the migration of water-ice in Martian polar regions[42]. During the regional dust storm, InSight's pressure sensor detected a sharp increase of the pressure slope with time that

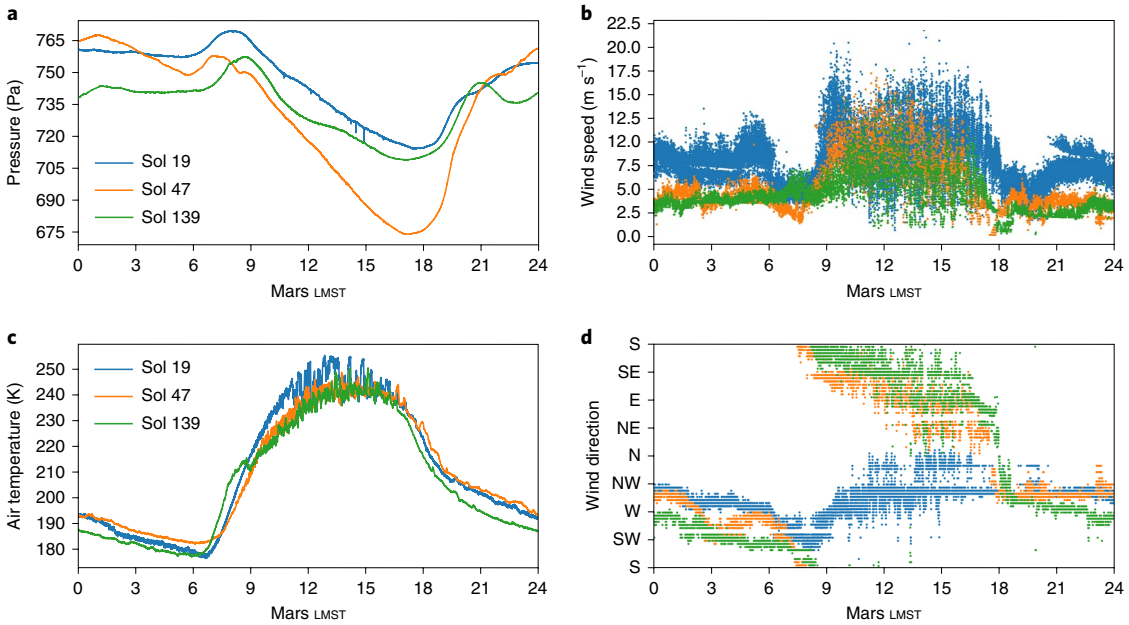

Fig. 2 | The Martian meteorology of three typical sols experienced by InSight shows a diversity of scales involved from the planetary scale to local turbulent scales. a–d, Measurements of pressure (**a**), wind speed (**b**), atmospheric temperature (**c**) and wind direction (**d**) are shown. The blue lines correspond to sol 19, shortly after landing ($L_s = 307°$). The orange lines correspond to sol 47 during the regional dust storm, which significantly perturbed the local weather at the InSight landing site ($L_s = 324°$). The green lines correspond to sol 139 ($L_s = 13°$) in northern spring after the decay of the regional dust storm. The directions indicated for winds are the directions from which the wind is blowing, following atmospheric science convention.

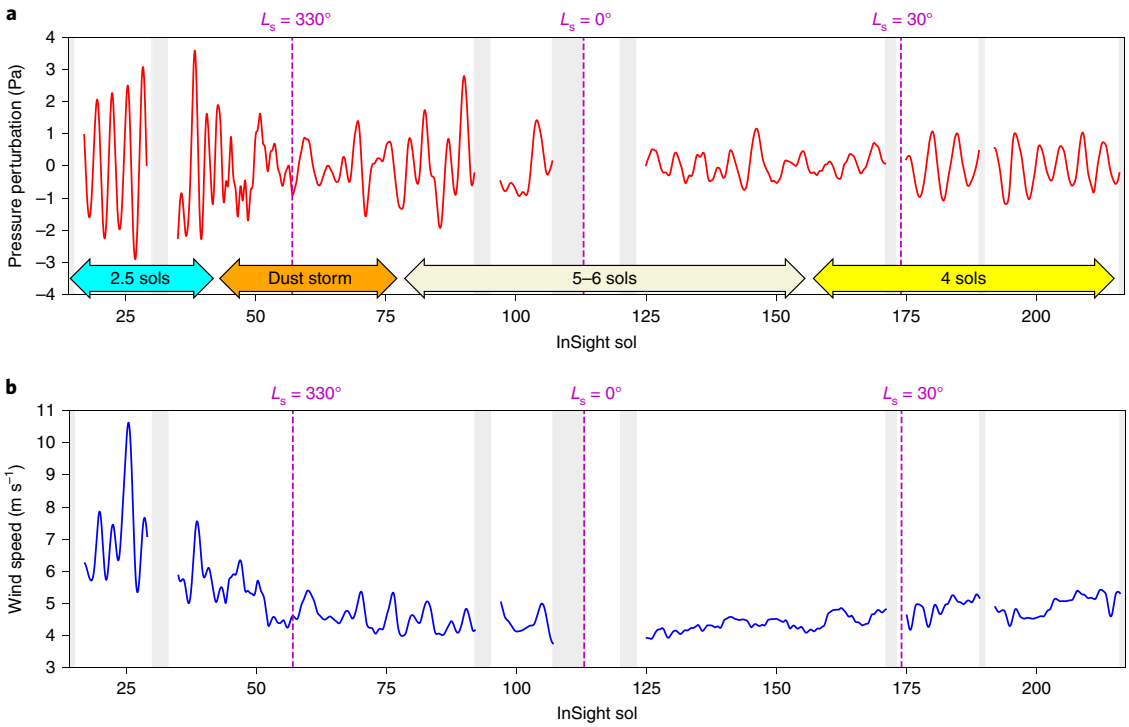

Fig. 3 | Despite its equatorial location, InSight's pressure and wind daily variability are sensitive to the weather in Mars's mid-latitudes, dominated by baroclinic instability. a,**b**, Pressure (**a**) and wind (**b**) fluctuations obtained by low-pass filtering to remove thermal tides, mesoscale meteorology and local turbulence signals. Pressure is also detrended with a 1 sol running mean, which removes the seasonal impact of CO_2 condensation and/or sublimation. Grey areas correspond to sol intervals during which APSS (Auxiliary Payload Sensor Suite) experienced anomalies that prevented measurements from being carried out. Wavelet analysis of the excerpts of the pressure signal in **a** are shown in Extended Data Fig. 3.

occurred every sol in early evening, which then grew into pressure 'bumps' in the storm's decaying phase. The pressure bumps reached a maximum of 4 Pa, and occurred later and later every sol (for reasons not yet understood) before decreasing and disappearing at the end of the dust storm disturbance (Fig. 4b). They were followed by 900 s period fluctuations of pressure and air temperature as well

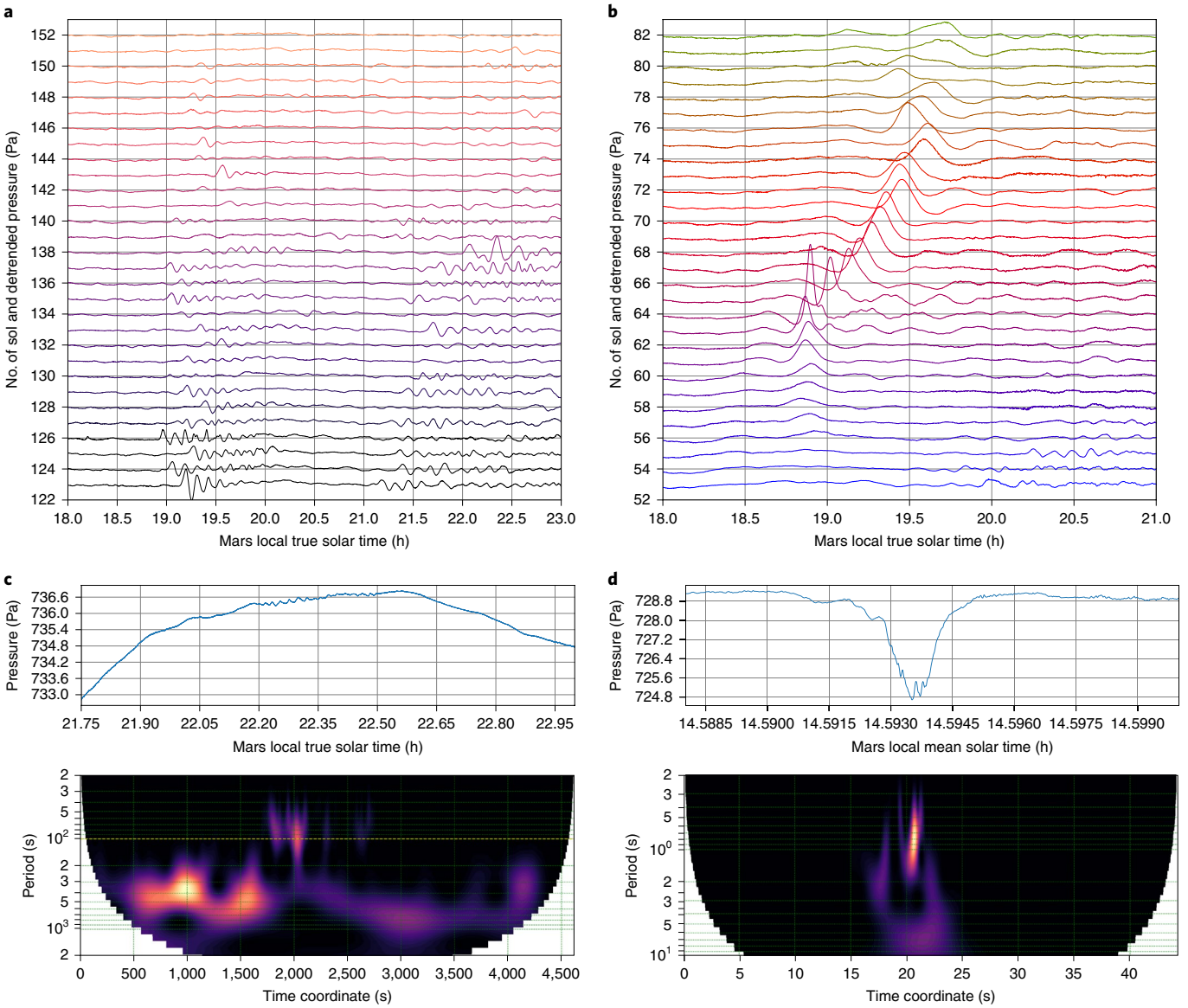

Fig. 4 | InSight unveiled pressure fluctuations probably related to gravity waves, bores and solitary waves and infrasound. a,**b**, Pressure fluctuations probably related to gravity waves (**a**), and bores and solitary waves (**b**). The pressure was detrended using a 2,000 s smoothing window in evening conditions. The *x* axis is the local true solar time in Martian hours. The *y* axis follows the pulsar plot by Craft[65], which was used as the cover of Joy Division's *Unknown Pleasures* album: each line corresponds to a sol and the vertical scale is the detrended pressure (Pa) offset by the sol number. **c**, Pressure measurements during an evening gravity-wave event on sol 78 ($L_s = 341°$) above a wavelet power spectra of the signal detrended using a 500 s smoothing window. The yellow line shows the 100 s period below which oscillations are infrasound rather than gravity waves. **d**, Same as **c**, but during a daytime vortex-induced pressure drop on sol 26 ($L_s = 311°$) using a 2 s smoothing window to isolate the infrasound from the convective vortex.

as changes in wind speed and direction. For InSight, the density current that causes the bore could be katabatic drainage flows coming from the slopes of Elysium Mons and/or the dichotomy boundary. Dust storm conditions on Mars reinforce the night-time low-level jet[43], which is known to be a near-surface trapping mechanism for wave energy conducive to bores[44]. Pressure jumps in the morning were also observed on at least one sol after the complete decay of the dust storm, which suggest bores might also occur in clear seasons.

Atmospheric oscillations at higher frequencies than gravity waves belong to the acoustic regime, not explored on Mars prior to InSight. Benefiting from unprecedented fine-sensitivity and high-frequency coverage, InSight's pressure sensor revealed coherent oscillations that are candidates for infrasound—acoustic waves at frequencies less than ~20 Hz, which may propagate over large distances[45]. The first type of candidate infrasound includes, embedded within a 300–500 s gravity-wave signal, additional night-time pressure oscillations of period 80 s (Fig. 4c), slightly below the lower-limit gravity-wave period of ~100 s in the observed conditions. The second type of candidate infrasound are pressure oscillations with a period of ~0.8 s occasionally found within the pressure minimum of daytime convective vortices (Fig. 4d).

Turbulence studies

Convective vortices are key phenomena during the daytime turbulent regime and are termed dust devils if their dust content makes them visible. InSight is the most active site for convective vortices visited thus far by a spacecraft carrying a pressure sensor. About

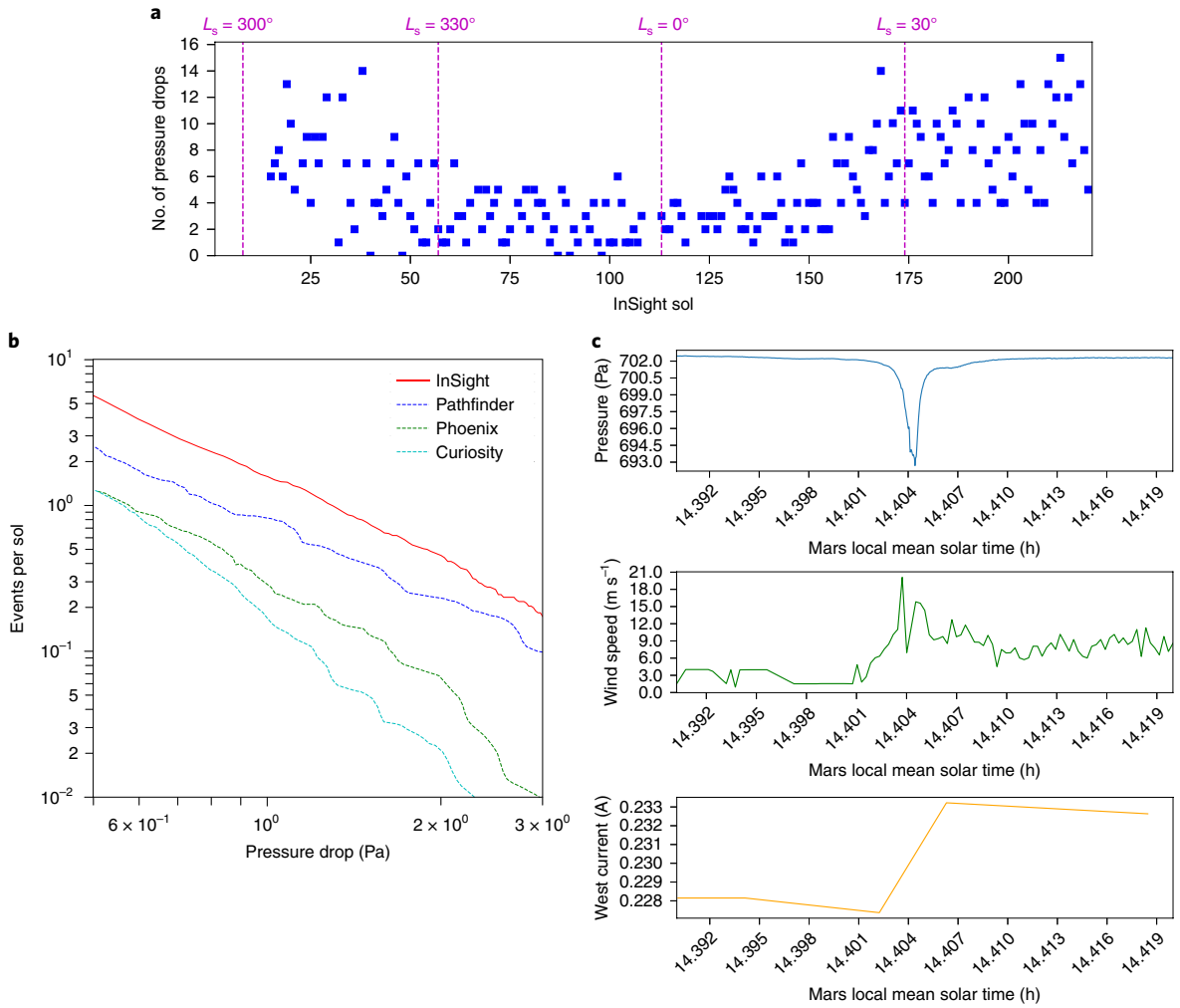

Fig. 5 | Daytime dust-devil-like convective vortices are very active at the InSight landing site and caused at least one solar-panel cleaning event witnessed by InSight. a, Number of pressure drops per sol that exceeded 0.5 Pa (the list of the 15 strongest events is included as Extended Data Fig. 7). **b**, Distribution of pressure drops per sol, normalized by diurnal coverage and number of observed sols, including the statistics from other landers[46–48]. **c**, Pressure, wind speed and solar array current recorded during the deepest pressure drop observed at the surface of Mars thus far (InSight sol 65, $L_s = 334°$).

1,000 sudden pressure drop events deeper than 0.5 Pa, which correspond to convective vortices, were detected during InSight's first 220 sols (Fig. 5a). InSight detected about twice as many vortices per sol as Pathfinder[46] and up to five times as many as Phoenix[47] and Curiosity[48], accounted for by their respective temporal coverage (Fig. 5b). This strong vortex activity caused ground deformations recorded in seismic measurements[49,50] and provided a natural seismic source to probe the first few metres below the surface[11]—magnetic signatures are ambiguous[51]. On sol 65, when a 9 Pa pressure drop passed over the lander (the strongest convective vortex measured to date on Mars), InSight recorded a sudden 1% increase in solar power (Fig. 5c), putatively caused by dust being removed from the solar panels, and imaged clumps of particles that had moved on InSight's wind and thermal shield. Orbital HiRISE imaging[52] of ~100 km^2 around the InSight landing site has also revealed tens of newly formed dust-devil tracks in a short 5 sol window after InSight's landing, when intense vortex activity was detected by the pressure sensor. The inferred production rate for these tracks is ~0.57 tracks sol^{-1} km^{-2}, an order of magnitude larger than the pre-landing predictions[53]. Sol-to-sol linear or curvilinear changes in surface brightness have also occasionally been seen by taking ratios of InSight images at a similar illumination[54].

Nevertheless, InSight shows that the mobilization of dust particles from the surface is a subtle process. During the strongest wind gust recorded by InSight's wind sensors (~24 m s^{-1} on sol 26), no associated motion of dust particles could be robustly demonstrated. Furthermore, not a single dust devil has been imaged from the ground in the first 200 sols of the mission, even though hundreds of mid-day Instrument Context Camera (ICC) and tens of IDC images (including periods with many vortex-pressure-drop detections) have been analysed. If vortices lifted dust as often at InSight as at, for example, the Spirit landing site[55], at least several dust devils (if not dozens) should have been imaged. The formation of dust-devil tracks means that at least enough dust is being lifted by vortices to change the surface albedo. Yet it appears that either the amount of dust lifted is insufficient to produce dust devils visible to InSight's cameras, which would differ from other sites with similar (or even far less) vortex activity, or that InSight has simply missed seeing them due to the timing and number of observations made to date. On a more general note, InSight's potential to contribute to aeolian science will be fully expressed with a coverage over a full Martian year of wind speeds, pressure drops and surface change images[56].

The repeated continuous measurements by InSight, both atmospheric (Fig. 2) and seismic[12,57], strongly suggest, in addition to the

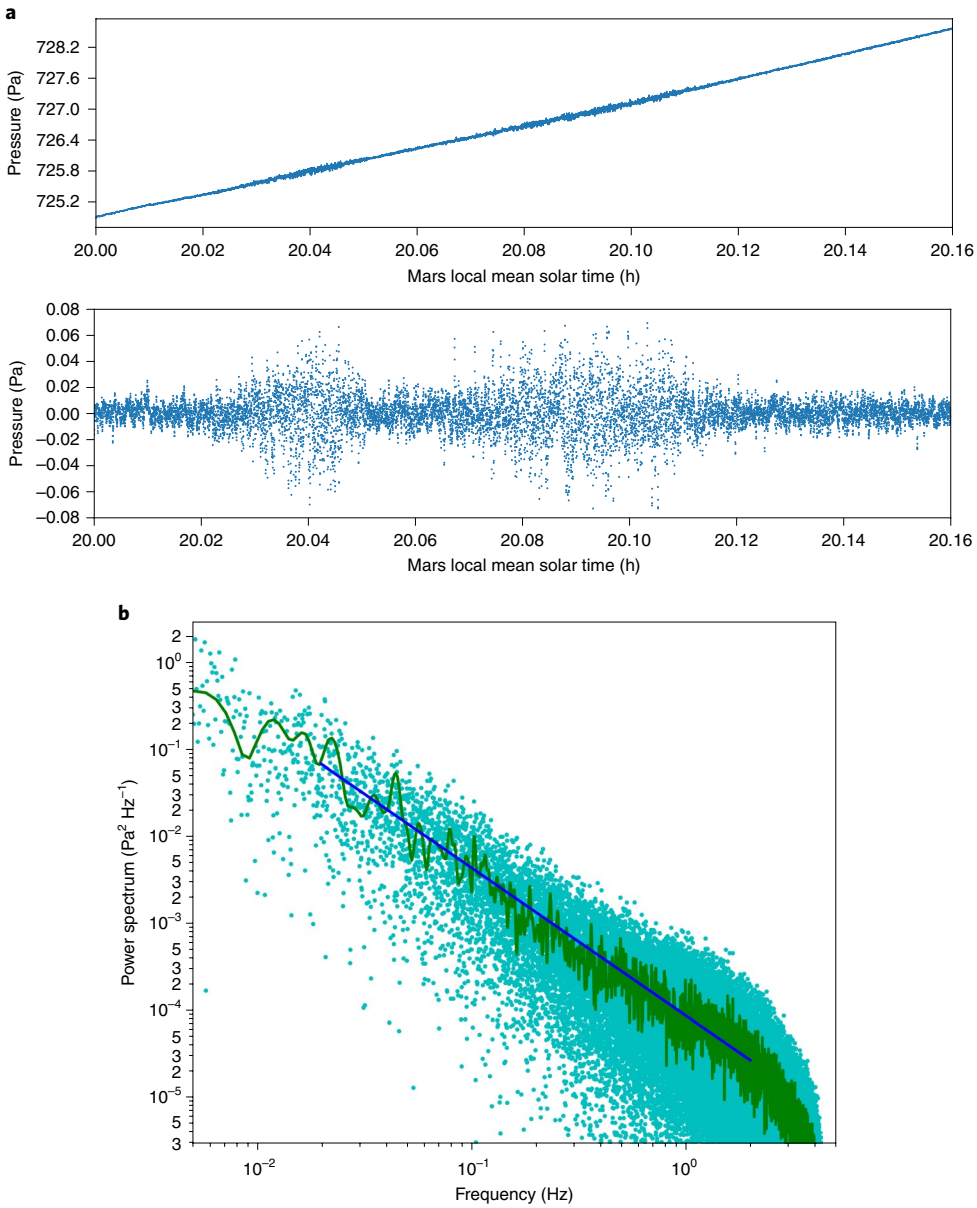

Fig. 6 | The InSight pressure sensor explores a new territory of high-frequency turbulence on Mars. a, High-frequency pressure bursts detected on sol 114 ($L_s = 0°$): the raw pressure signal is shown on top of a detrended version using a smoothing window of 50 s. **b**, Power spectrum produced from 40 sols of daytime pressure fluctuations from sols 168 to 208 ($L_s = 27–45°$) when pressure was continuously sampled at 10 Hz. Cyan points correspond to the spectra computed for InSight pressure measurements. The green curve is a smoothed version of the cyan points to display the average power spectrum of pressure more clearly. A power-law fitting ($f(x) = ax^b$ with $b = -1.70$) of the data points in cyan in the range 0.02–2 Hz is shown as a blue line.

two aforementioned previously known daytime/night-time turbulent regimes, the existence of a new, third 'quiet' regime: both the ambient and turbulent wind speed are systematically extremely low about 2-4 hours after sunset (Fig. 2b and Extended Data Fig. 8), following the collapse of daytime turbulence. This has remained elusive in previous measurements that lacked InSight's resolution and continuity[4]. The transition from the daytime convective regime to the evening quiet regime is very abrupt, much more than that experienced on Earth, and results from the efficient radiative cooling of the surface and the near-surface Martian atmosphere at sunset—interestingly, during the dusty sols 40–90, not only was the daytime turbulence reduced (Fig. 2b) but also the quiet regime was less clearly defined (Extended Data Fig. 8). The later transition from the evening quiet regime to the night time shear-driven regime is more gradual and corresponds to the onset of the nocturnal low-level jet[28,43]: as the nocturnal thermal inversion develops, the winds above become decoupled from the surface and the decrease in friction produces a net acceleration. Interestingly, a quiet regime akin to the evening regime is occasionally also observed a couple of hours before sunrise. The quiet regime identified by InSight has proved to be of paramount importance for seismic detection. The atmosphere is the major source of seismic noise on Mars[11], so a strong ambient wind and/or strong turbulence significantly increases the detection threshold for Mars quakes[12]. As a result, the vast majority of seismic events are detected specifically during the quiet regime.

The InSight pressure measurements at a high frequency yield novel results for turbulence compared to those of existing studies on Mars[30,58]. Night-time high-frequency fluctuations of pressure, wind and air temperature are found by InSight to be typically 2–10 times smaller than those in the daytime regime (Extended Data Fig. 8a).

Significant sol-to-sol variability in the intensity and peak timing of the night-time turbulence is experienced at InSight, the most remarkable phenomenon being the irregular occurrence of 'pressure bursts' in the high-frequency 2–10 Hz range (Fig. 6a), which show no correlation with any instrument artefacts or lander events. Such intermittent turbulence is also found on Earth in peculiar highly stable and low ambient wind conditions[59], which are also met during the InSight pressure burst observations.

Mars is an interesting laboratory to study daytime turbulence on a purely theoretical basis—compared to Earth, the Martian daytime turbulence is characterized by a stronger radiative control, a lack of latent heat forcing and a reduced inertial range[60]. The high-frequency pressure measurements performed by InSight during numerous sols in this much different Martian environment can be compared to turbulent pressure spectra measured on Earth[61,62], which contradict the inertial subrange predictions for pressure by the classical Kolmogorov theory. The power spectral density of pressure measured by InSight in the daytime (Fig. 6b) can be described consistently for frequencies f from 5×10^{-2} Hz to 2 Hz with a power law f^{α} such that $\alpha = -1.7$. Despite the environmental differences between Mars and Earth, this exponent slope retrieved by InSight is remarkably similar to exponent slopes α from −1.5 to −1.7 retrieved on Earth. Hence, both the terrestrial and Martian measurements concur to show that the −7/3 ($\simeq -2.33$) slope expected for pressure from the Kolmogorov theory[63] is not supported by in situ observations. This strongly suggests that, contrary to wind and temperature, a combined influence of local turbulence and larger-scale variability is needed to account for high-frequency pressure fluctuations[62].

Online content

Any methods, additional references, Nature Research reporting summaries, source data, extended data, supplementary information, acknowledgements, peer review information; details of author contributions and competing interests; and statements of data and code availability are available at https://doi.org/10.1038/s41561-020-0534-0.

Received: 29 August 2019; Accepted: 7 January 2020;
Published online: 24 February 2020

References

1. Haberle, R. M., Clancy, R. T., Forget, F., Smith, M. D. & Zurek, R. W. *The Atmosphere and Climate of Mars* Vol. 18 (Cambridge Univ. Press, 2017).
2. Hess, S. L., Henry, R. M., Leovy, C. B., Ryan, J. A. & Tillman, J. E. Meteorological results from the surface of Mars: Viking 1 and 2. *J. Geophys. Res.* **82**, 4559–4574 (1977).
3. Clancy, R. T. & Sandor, B. J. CO_2 ice clouds in the upper atmosphere of Mars. *Geophys. Res. Lett.* **25**, 489–492 (1998).
4. Martínez, G. M. et al. The modern near-surface Martian climate: a review of in-situ meteorological data from Viking to Curiosity. *Space Sci. Rev.* **212**, 295–338 (2017).
5. Haberle, R. M. et al. Preliminary interpretation of the REMS pressure data from the first 100 sols of the MSL mission. *J. Geophys. Res. Planets* **119**, 440–453 (2014).
6. Banfield, D. et al. InSight Auxiliary Payload Sensor Suite (APSS). *Space Sci. Rev.* **215**, 4 (2018).
7. Spiga, A. et al. Atmospheric science with insight. *Space Sci. Rev.* **214**, 109 (2018).
8. Schofield, J. T. et al. The Mars Pathfinder atmospheric structure investigation/meteorology (ASI/MET) experiment. *Science* **278**, 1752–1757 (1997).
9. Holstein-Rathlou, C. et al. Winds at the Phoenix landing site. *J. Geophys. Res. Planets* **115**, E00E18 (2010).
10. Gómez-Elvira, J. et al. Curiosity's rover environmental monitoring station: overview of the first 100 sols. *J. Geophys. Res. Planets* **119**, 1680–1688 (2014).
11. Lognonné, P. et al. Constraints on the shallow elastic and anelastic structure of Mars from InSight seismic data. *Nat. Geosci.* https://doi.org/10.1038/s41561-020-0536-y (2020).
12. Giardini, D. et al. The seismicity of Mars. *Nat. Geosci.* https://doi.org/10.1038/s41561-020-0539-8 (2020).
13. Barnes, J. R. Time spectral analysis of the midlatitude disturbances in the Martian atmosphere. *J. Atmos. Sci.* **37**, 2002–2015 (1980).
14. Banfield, D., Conrath, B. J., Gierasch, P. J., Wilson, R. J. & Smith, M. D. Traveling waves in the Martian atmosphere from MGS TES Nadir data. *Icarus* **170**, 365–403 (2004).
15. Collins, M., Lewis, S. R., Read, P. L. & Hourdin, F. Baroclinic wave transitions in the Martian atmosphere. *Icarus* **120**, 344–357 (1996).
16. Lewis, S. R. et al. The solsticial pause on Mars: 1. A planetary wave reanalysis. *Icarus* **264**, 456–464 (2016).
17. Haberle, R. M. et al. Detection of Northern Hemisphere transient eddies at Gale Crater Mars. *Icarus* **307**, 150–160 (2018).
18. Ryan, J. A. & Henry, R. M. Mars atmospheric phenomena during major dust storms as measured at surface. *J. Geophys. Res.* **84**, 2821–2829 (1979).
19. Sánchez-Lavega, A., del Río-Gaztelurrutia, T., Hernández-Bernal, J. & Delcroix, M. The onset and growth of the 2018 Martian global dust storm. *Geophys. Res. Lett.* **46**, 6101–6108 (2019).
20. Murphy, J. R. et al. Three-dimensional numerical simulation of Martian global dust storms. *J. Geophys. Res.* **100**, 26357–26376 (1995).
21. Battalio, M., Szunyogh, I. & Lemmon, M. Energetics of the Martian atmosphere using the Mars Analysis Correction Data Assimilation (MACDA) dataset. *Icarus* **276**, 1–20 (2016).
22. Määttänen, A. et al. Mapping the mesospheric CO_2 clouds on Mars: MEx/OMEGA and MEx/HRSC observations and challenges for atmospheric models. *Icarus* **209**, 452–469 (2010).
23. Clancy, R. T. et al. The distribution, composition, and particle properties of Mars mesospheric aerosols: an analysis of CRISM visible/near-IR limb spectra with context from near-coincident MCS and MARCI observations. *Icarus* **328**, 246–273 (2019).
24. Scholten, F. et al. Concatenation of HRSC colour and OMEGA data for the determination and 3D-parameterization of high-altitude CO_2 clouds in the Martian atmosphere. *Planet. Space Sci.* **58**, 1207–1214 (2010).
25. Sonnabend, G., Sornig, M., Kroetz, P. & Stupar, D. Mars mesospheric zonal wind around northern spring equinox from infrared heterodyne observations of CO_2. *Icarus* **217**, 315–321 (2012).
26. Gronoff, G. et al. Computing uncertainties in ionosphere–airglow models: ii. The Martian airglow. *J. Geophys. Res. Space Phys.* **117**, A05309 (2012).
27. Zurek, R. W. & Leovy, C. B. Thermal tides in the dusty Martian atmosphere—a verification of theory. *Science* **213**, 437–439 (1981).
28. Savijärvi, H. & Siili, T. The Martian slope wind and the nocturnal PBL jet. *J. Atmos. Sci.* **50**, 77–88 (1993).
29. Spiga, A. et al. The impact of Martian mesoscale winds on surface temperature and on the determination of thermal inertia. *Icarus* **212**, 504–519 (2011).
30. Tillman, J. E., Landberg, L. & Larsen, S. E. The boundary layer of Mars: fluxes stability, turbulent spectra and growth of the mixed layer. *J. Atmos. Sci.* **51**, 1709–1727 (1994).
31. Lee, C. et al. Thermal tides in the Martian middle atmosphere as seen by the Mars Climate Sounder. *J. Geophys. Res. Planets* **114**, E03005 (2009).
32. Wilson, R. W. & Hamilton, K. Comprehensive model simulation of thermal tides in the Martian atmosphere. *J. Atmos. Sci.* **53**, 1290–1326 (1996).
33. Fritts, D. C. & Alexander, M. J. Gravity wave dynamics and effects in the middle atmosphere. *Rev. Geophys.* **41**, 1003 (2003).
34. Barnes, J. R. Possible effect of breaking gravity waves on the circulation of the middle atmosphere of Mars. *J. Geophys. Res.* **95**, 1401–1421 (1990).
35. Magalhaes, J. A., Schofield, J. T. & Seiff, A. Results of the Mars Pathfinder atmospheric structure investigation. *J. Geophys. Res.* **104**, 8943–8956 (1999).
36. Creasey, J. E., Forbes, J. M. & Hinson, D. P. Global and seasonal distribution of gravity wave activity in Mars' lower atmosphere derived from MGS radio occultation data. *Geophys. Res. Lett.* **33**, L01803 (2006).
37. Spiga, A. et al. Remote sensing of surface pressure on Mars with the Mars Express/OMEGA spectrometer: 2. Meteorological maps. *J. Geophys. Res. Planet* **112**, E08S16 (2007).
38. Harri, A.-M. et al. Pressure observations by the Curiosity Rover: initial results. *J. Geophys. Res. Planets* **119**, 82–92 (2014).
39. Rafkin, S. C. R. et al. The meteorology of Gale Crater as determined from Rover Environmental Monitoring Station observations and numerical modeling. part ii: Interpretation. *Icarus* **280**, 114–138 (2016).
40. Hartung, D. C., Otkin, J. A., Martin, J. E. & Turner, D. D. The life cycle of an undular bore and its interaction with a shallow, intense cold front. *Monthly Weather Review* **138**, 886–908 (2010).
41. Maria, M. R. V. S., Rafkin, S. C. R. & Michaels, T. I. Numerical simulation of atmospheric bore waves on Mars. *Icarus* **185**, 383–394 (2006).
42. Spiga, A. & Smith, I. Katabatic jumps in the Martian northern polar regions. *Icarus* **308**, 197–208 (2018).
43. Joshi, M. M., Haberle, R. M., Barnes, J. R., Murphy, J. R. & Schaeffer, J. Low-level jets in the NASA Ames Mars general circulation model. *J. Geophys. Res. Planets* **102**, 6511–6524 (1997).
44. Koch, S. E. et al. Structure of an internal bore and dissipating gravity current as revealed by Raman lidar. *Monthly Weather Rev.* **119**, 857–887 (1991).
45. Williams, J.-P. Acoustic environment of the Martian surface. *J. Geophys. Res.* **106**, 5033–5042 (2001).

46. Murphy, J. R. & Nelli, S. Mars Pathfinder convective vortices: frequency of occurrence. *Geophys. Res. Lett.* **29**, 2103 (2002).
47. Ellehoj, M. D. et al. Convective vortices and dust devils at the Phoenix Mars mission landing site. *J. Geophys. Res. Planets* **115**, E00E16 (2010).
48. Ordonez-Etxeberria, I., Hueso, R. & Sánchez-Lavega, A. A systematic search of sudden pressure drops on Gale Crater during two Martian years derived from MSL/REMS data. *Icarus* **299**, 308–330 (2018).
49. Lorenz, R. D. et al. Seismometer detection of dust devil vortices by ground tilt. *Bull. Seismol. Soc. Am.* **105**, 3015–3023 (2015).
50. Kenda, B. et al. Modeling of ground deformation and shallow surface waves generated by Martian dust devils and perspectives for near-surface structure inversion. *Space Sci. Rev.* **211**, 501–524 (2017).
51. Johnson, C. L. et al. Crustal and time-varying magnetic fields at the InSight landing site on Mars. *Nat. Geosci.* https://doi.org/10.1038/s41561-020-0537-x (2020).
52. McEwen, A. S. et al. Mars Reconnaissance Orbiter's High Resolution Imaging Science Experiment (HiRISE). *J. Geophys. Res.* **112**, E05S02 (2007).
53. Reiss, D. & Lorenz, R. D. Dust devil track survey at Elysium Planitia, Mars: implications for the InSight landing sites. *Icarus* **266**, 315–330 (2016).
54. Banerdt, W. B. et al. Initial results from the InSight mission on Mars. *Nat. Geosci.* https://doi.org/10.1038/s41561-020-0544-y (2020).
55. Greeley, R. et al. Gusev Crater, Mars: observations of three dust devil seasons. *J. Geophys. Res. Planets* **115**, E00F02 (2010).
56. Golombek, M. et al. Geology of the InSight landing site on Mars. *Nat. Commun.* https://doi.org/10.1038/s41467-020-14679-1 (2020).
57. Lognonné, P. et al. SEIS: InSight's Seismic Experiment for Internal Structure of Mars. *Space Sci. Rev.* **215**, 12 (2019).
58. Davy, R. et al. Initial analysis of air temperature and related data from the Phoenix MET station and their use in estimating turbulent heat fluxes. *J. Geophys. Res. Planets* **115**, E00E13 (2010).
59. Van de Wiel, B. J. H., Ronda, R. J., Moene, A. F., de Bruin, H. A. R. & Holtslag, A. A. M. Intermittent turbulence and oscillations in the stable boundary layer over land Part I: a bulk model. *J. Atmos. Sci.* **59**, 942–958 (2002).
60. Larsen, S. E., Jørgensen, H. E. & Landberg, L. et al. Aspects of the atmospheric surface layers on Mars and Earth. *Bound. Lay. Meteorol.* **105**, 451–470 (2002).
61. Elliott, J. A. Microscale pressure fluctuations measured within the lower atmospheric boundary layer. *J. Fluid Mech.* **53**, 351–383 (1972).
62. Albertson, J. D., Katul, G. G., Parlange, M. B. & Eichinger, W. E. Spectral scaling of static pressure fluctuations in the atmospheric surface layer: the interaction between large and small scales. *Phys. Fluids* **10**, 1725–1732 (1998).
63. Tsuji, Y., Fransson, J. H. M., Alfredsson, P. H. & Johansson, A. V. Pressure statistics and their scaling in high-Reynolds-number turbulent boundary layers. *J. Fluid Mech.* https://doi.org/10.1017/S0022112007006076 (2007)..
64. Withers, P. & Smith, M. D. Atmospheric entry profiles from the Mars Exploration Rovers Spirit and Opportunity. *Icarus* **185**, 133–142 (2006).
65. Craft, H. D. Jr *Radio Observations of the Pulse Profiles and Dispersion Measures of Twelve Pulsars*. PhD thesis, Cornell Univ. (1970).

Methods

Mars calendars and times. The Mars–Sun angle, named the solar longitude L_s (°), is used to indicate seasons on Mars: 0° corresponds to northern spring equinox, 90° to northern summer solstice (aphelion season), 180° to northern fall equinox and 270° to northern winter solstice (perihelion season). A Mars solar year is about 1.9 Earth years, or 668.59 sols. The InSight landing on 26 November 2018 corresponds to InSight sol 0. Extended Data Fig. 2 indicates the correspondence between InSight sols and L_s. Mars local mean solar time is measured by using a 24 h 'Mars clock', in which the timing of local noon undergoes a seasonal variation of up to 50 min. Mars local true solar time (LTST) indicates the sundial hours: noon always corresponds to a zenith position of the sun in the sky.

Atmospheric profiles during EDL. InSight's EDL trajectory and associated atmospheric structure was reconstructed using data from its accelerometers and gyroscopes, following a method similar to that developed for Phoenix's EDL trajectory[66]. Details of the method are provided in Section 3.1 of the prelanding paper[7].

Pressure measurements. The pressure sensor on board InSight samples at 20 Hz with a noise level of 10 mPa $Hz^{-1/2}$ from 0.1 to 1 Hz rising to 50 mPa $Hz^{-1/2}$ at 0.01 Hz have, respectively, one order of magnitude higher frequency and two orders of magnitude finer resolution than those previous instruments sent to Mars[4,6]. The pressure sensor communicates with the ambient atmosphere through an inlet tubing[6] specifically designed to minimize the effects of wind on the pressure measurements. Nevertheless, the variance of the pressure signal measured by InSight at frequencies above 2 Hz is sometimes correlated with wind speed, which potentially points towards either a loss of effectiveness of the pressure inlet at such frequencies or to mechanical or electrical noise within the pressure sensor; as a result, although future work might extract useful information from the pressure measurements above 2 Hz, our discussions are based only on frequencies below this limit (for example, as in Fig. 6b). A notable exception is the occurrence of night time high-frequency pressure bursts reported in Fig. 6a, which are not correlated with wind speed.

Wind and temperature measurements. The TWINS sensor booms, based on the same principle as those on board the Curiosity rover, face outward over InSight's two solar panels at ~1.2 m from the surface (respectively, 121.5 and 111.5 cm from the surface for the west and east booms, due to InSight's tilt) to acquire wind and air temperature at a frequency of 1 Hz and an accuracy of ~1 m s^{-1} for wind speed, 22.5° for wind direction and 5 K for temperature. Wind speed and direction are reconstructed given the measurements of the two booms, the position of each boom compared to the prevailing wind and corrections of the influence of lander elements on the retrieved wind, as obtained from computational fluid dynamics simulations. Details on wind measurements are provided in the prelanding references[6,7]. Wind retrievals are not reliable for Reynolds numbers Re $\lesssim$ 50, and sometimes questionable for Re $\lesssim$ 90, which corresponds to wind speeds, respectively, of 1.8 and 2.8 m s^{-1} at the pressure and temperature conditions experienced by InSight.

The air temperature measurements are perturbed from measuring a clean, true air temperature measurement due their close proximity to the lander itself (for example, from ultracooled solar panels during the night) and their non-negligible radiative cross-section. When winds and convection are strong, the advective heat transfer to the sensor dominates, but when winds are low, radiative effects are more significant. Discrepancy from the modelling suggests that these perturbations may reach as high as 10–15 K. The air temperature measurements by TWINS appear to be not perturbed equally at different local times: in daytime, differences between the two booms are very high, while at night, measurements by the two booms are close to one another but exhibit a spurious offset to yield air temperatures unphysically colder than the surface temperatures retrieved by InSight's radiometer. Further work is warranted to fully understand this issue.

Measurements by major InSight instruments of interest for atmospheric science. The InSight instrument suite for atmospheric science also includes a radiometer within the Heat Flow and Physical Properties Package (HP^3) to measure surface brightness temperature[56,67]. For the first time on Mars, InSight includes the ability to use the wind- and pressure-induced perturbations from seismic measurements by SEIS for atmospheric science[7,11,12,57] with (from sol 66) the wind and thermal shield that covers InSight's seismometer where it sits on the surface. The description of the methodology developed for seismic data is included in the SEIS companion papers[11,12].

Imaging in situ and from orbit. The two cameras on board InSight[68] (the IDC on the forearm with a 45° field-of-view and the ICC just below the deck with a 180° field-of-view) can image the sky to perform regular dust opacity estimates (the method is detailed in the Section 3.3.2 of the prelanding reference[7]) and occasional surveys for dust devils and clouds. The reported HiRISE (High Resolution Imaging Science Experiment) images have the following references: ESP 057939 1845 (6 December 2018), ESP 058005 1845 (11 December 2018) and ESP 060695 1845 (8 July 2019). A simple ratio was performed between co-registered HiRISE images to bring out new surface changes, such as dust-devil tracks. Then, both manual mapping and semi-automatic track detections using the radon transform technique were performed to characterize the main track properties (for example, azimuth, distance to lander, width and so on).

Noctilucent clouds. The noctilucent clouds were found in a set of images taken after the Sun had set at the lander (around 18:30 local time), but the terminator still intercepted the atmosphere at an altitude of 50 km. The fact that the clouds were illuminated reveals their height as at least 50 km. The images were map projected onto a spherical shell 50 km above the mean surface level and the motion of discrete features was measured in the projected image.

Airglow detection. The airglow detection was made in a series of four IDC images taken from 22:06 to 22:47 local true solar time on sol 126, with the Sun roughly 60° below the horizon. The images had 5 min exposure times and were dark corrected and co-added. The shadow of the scoop was clearly visible, which demonstrates the existence of skylight as opposed to an unmodelled dark current. The relative brightness of the excess light in the three broadband colour channels of InSight's cameras was not diagnostic, but is consistent with a 577.8 nm emission and not consistent with starlight or moonlight.

Dust-devil imaging non-detection. As of sol 200, 655 ICC images were taken with the Sun up; of these, 278 were taken with the Sun above 45° and 443 were taken over 11–17 LTST. At least ten of the ICC images were taken within 5 min of a vortex with a recorded pressure drop >1 Pa. We examined ratios of these images to images that were nearby in a metric that combined time of day (for illumination) and sol (for dust on the optics). No features were seen at the percentage level for high compression quality images (the large majority) or at the several percentage level in low-quality images. In addition, 333 IDC images including the horizon were examined, of which 90% were taken from 11 to 17 LTST and half were taken with the Sun above 45° elevation. These were primarily aimed to the south-southeast to south-southwest, with eastward directions rarely sampled. Similar processing that used an average of sky images for comparison yielded no dust-devil-like features at subpercentage levels.

Atmospheric modelling. The predictions by global climate modelling used for this study are referenced in Section 2.2 of the prelanding paper[7]. The method used to extrapolate the wind speed from the first model levels above the surface to the level of the TWINS measurements used the formalism described in Section 6.1 of the prelanding paper[7]. The global climate model simulation with flattened topography mentioned in the text and presented in Extended Data Fig. 4 was carried out in the exact same setting defined in the prelanding paper[7], except for a flattening of the topographical slopes over a box 10° of latitude and longitude centred at the InSight landing site.

Signal processing. To perform low-pass or high-pass filtering of the signal, time series of InSight measurements were smoothed using a one-dimensional convolution approach with a Hanning window, as is described in the cookbook of the `scipy` Python package https://scipy-cookbook.readthedocs.io/items/SignalSmooth.html. The spectral analysis carried out in this paper uses the wavelet approach adapted to atmospheric science described in the reference study on this topic[69] with details included in http://paos.colorado.edu/research/wavelets (the Python version adapted by E. Predybaylo is used in this study). Detailed information on the codes used for the analysis in this paper are provided in the Code availability section.

Seasonal variations of pressure. CO_2 is the main component of the Martian atmosphere and the surface pressure on Mars varies on a seasonal basis up to 30% as a result of the condensation and sublimation of the CO_2 in Martian polar regions[2]. Over the timespan of about a quarter of a Martian year covered by the initial InSight measurements, the general pressure trend is a long-term decrease in northern winter caused by condensation of CO_2 in the northern seasonal polar cap, followed by an increase due to sublimation in northern spring. This evolution closely follows the Viking observations 40 years ago, once corrected for topography and atmospheric dynamics[7,70].

Diurnal cycle of wind direction. The InSight wind measurements indicate a northwesterly wind in northern winter, slowly transitioning in northern spring to a southeasterly wind only in the daytime (Fig. 2d), consistent with dust-devil tracks and ripples in Elysium Planitia[53,71]. The measured wind behaviour confirms the pre-landing predictions by global climate modelling[7] in the Elysium Planitia region, which points to the combined influence of Hadley cells and western boundary currents, two key phenomena that also control Earth's large-scale winds in the subtropics.

Gravity-wave analysis. The simultaneous detection of gravity-wave oscillations of pressure and wind by a surface weather station enables the horizontal wavelength of the putative gravity wave to be estimated[72]. The range of periods detected by InSight (less than half a Martian hour) corresponds to high-to-mid-frequency

gravity waves for which the Coriolis influence is negligible—an approximation also ensured by the equatorial position of InSight. In these conditions, according to the polarization equations[33], the pressure perturbation p' is related to the wind speed perturbation V' by the 'impedance relation'[72,73]:

$$V' = \frac{p'}{\rho_0 \ (c - V)}$$

where ρ_0 and V are, respectively, the ambient density and wind speed, and $c = \omega/k = \lambda/T$ is the phase speed of the gravity wave with ω and T the frequency and period and k and λ the horizontal wavenumber and wavelength. Oscillations of pressure and wind were simultaneously detected only in rare cases (4–5 clear-cut cases) in the first 200 sols of the InSight measurements; oscillations are more distinctively detected in the wind direction than in the wind speed. The wave packets identified in pressure and wind on sols 142 and 150 are included as representative examples in Extended Data Figs. 5 and 6. The gravity-wave period is found to be similar both in the pressure and wind time series; zonal wind, meridional wind and pressure are either in phase or 180° out of phase, which is compliant with polarization equations in the case of high-to-mid-frequency gravity waves (conversely, wind components in low-frequency inertio-gravity waves would be 90° out of phase). Once the period T is determined, the knowledge from InSight measurements of p' and V', as well as the ambient wind V, leads to the horizontal wavelength λ through the impedance relation (ambient InSight measurements of pressure and temperature yield $\rho_0 = 0.02\ \mathrm{kg\,m^{-3}}$). Horizontal wavelengths of 25 km and 33 km and phase speeds 17 $\mathrm{m\,s^{-1}}$ and 22 $\mathrm{m\,s^{-1}}$ were, respectively, found for sol 142 and sol 150 night-time wave packets. We checked that the non-linear version of the impedance relation[73] is not necessary because, in the cases studied here, the following linear approximation holds:

$$\rho_0 \frac{V'^2}{2} \ll p'$$

Data availability

The raw to calibrated datasets of InSight are available via the Planetary Data System (PDS). Data are delivered to the PDS according to the InSight Data Management Plan available in the InSight PDS archive. Data from the APSS pressure sensor and the temperature and wind (TWINS) sensor referenced in this paper are available from the PDS Atmospheres node. The direct link to the InSight data archive at the PDS Atmospheres node is https://atmos.nmsu.edu/data_and_services/atmospheres_data/INSIGHT/insight.html. Other data used in this paper are available from the imaging node (ICC and IDC images) and the geosciences node (SEIS and HP^3) of the PDS. SEIS data are also available from the Data center of Institut de Physique du Globe, Paris at https://doi.org/10.18715/SEIS.INSIGHT.XB_2016. Meteorology InSight data from the latest acquired sols can be found in the following user-friendly interface at https://mars.nasa.gov/insight/weather/.

Code availability

The Python codes developed to produce the figures directly from the InSight files in the PDS Atmospheres node are available in the online repository at https://github.com/aymeric-spiga/insight-atmosphere-nature-geoscience.

References

66. Withers, P. & Catling, D. C. Observations of atmospheric tides on Mars at the season and latitude of the Phoenix atmospheric entry. *Geophys. Res. Lett.* **37**, L24204 (2010).
67. Spohn, T. et al. The Heat Flow and Physical Properties Package (HP3) for the InSight Mission. *Space Sci. Rev.* **214**, 96 (2018).
68. Maki, J. N. et al. The color cameras on the InSight lander. *Space Sci. Rev.* **214**, 105 (2018).
69. Torrence, C. & Comp, G. P. A practical guide to wavelet analysis. *Bull. Am. Met. Soc.* **79**, 61–78 (1998).
70. Forget, F. et al. Remote sensing of surface pressure on Mars with the Mars Express/OMEGA spectrometer: 1. Retrieval method. *J. Geophys. Res. Planets* **112**, E08S15 (2007).
71. Golombek, M. et al. Geology and physical properties investigations by the InSight lander. *Space Sci. Rev.* **214**, 84 (2018).
72. Gossard, E. & Munk, W. On gravity waves in the atmosphere. *J. Meteorol.* **11**, 259–269 (1954).
73. Coleman, T. A. & Knupp, K. R. A nonlinear impedance relation for the surface winds in pressure disturbances. *J. Atmos. Sci.* **67**, 3409–3422 (2010).

Acknowledgements

All co-authors acknowledge NASA, CNES and its partner agencies and institutions (UKSA, SSO, DLR, JPL, IPGP-CNRS, ETHZ, IC and MPS-MPG) and the flight operations team at JPL, CAB, SISMOC, MSDS, IRIS-DMC and PDS for providing InSight data. The members of the InSight engineering and operations teams made the InSight mission possible and their hard work and dedication is acknowledged here. A portion of this research was carried out at the Jet Propulsion Laboratory, California Institute of Technology, under a contract with the National Aeronautics and Space Administration. Additional work was supported by NASA's InSight Participating Scientist Program. The French co-authors acknowledge the French Space Agency CNES, which funded scientific activities and supported SEIS-related contracts and CNES employees. Additional funding support was provided by Agence Nationale de la Recherche (ANR-14-CE36-0012-02 SIMARS and ANR-19-CE31-0008-08 MAGIS). Atmospheric modelling used HPC resources of CINES (Centre Informatique National de l'Enseignement Supérieur) under the allocations A0040110391 and A0060110391 attributed by GENCI (Grand Equipement National de Calcul Intensif). The Spanish co-authors acknowledge funding by the Centro de Desarrollo Tecnológico e Industrial (CDTI), Ministerio de Economía y Competitividad and the Instituto Nacional de Técnica Aeroespacial (INTA). The Swiss co-authors acknowledge funding by the Swiss National Science Foundation (SNF-ANR project 157133) and the Swiss State Secretariat for Education, Research and Innovation (SEFRI project MarsQuake Service-Preparatory Phase). The UK co-authors acknowledge funding by the UK Space Agency. This paper is InSight Contribution Number 103.

Author contributions

D.B. and A.S. equally led the investigations described here within the InSight Atmospheres Science Theme Group, carried out the analysis reported in this paper on all topics, submitted event request proposals related to atmospheric science and wrote the paper. C.N., F.F., D.V.-M., E.M. and S.R.L. analysed InSight meteorological data to support the large-scale weather studies. M.L, R.L., J.N.M. and A. Määttänen analysed InSight imaging and solar array data to support the dust aerosol and cloud studies. N.M., J.P.-G., R.F.G., L.M., B.K., L.R., R.W.-S., D.M. and K.H. analysed InSight meteorological data to support turbulence, gravity-wave and infrasound studies. P.L., N.T., T.K., J.B.M., A.E.S., T.W., W.T.P. and E.B. analysed InSight seismic data and submitted event request proposals to support the atmospheric science studies, especially related to turbulence. O.K. and B.V.H. analysed InSight EDL data to retrieve the entry profile. J.C., S.C.S., S.C. and D.G. routinely analysed InSight seismic and pressure data within the Mars Quake Service to detect atmospheric events. C.P., S.R., I.D., A.J. and A. Lucas analysed HiRISE images to support the dust devil tracks studies. N.T.M. and T.S. analysed InSight radiometer surface temperature measurements to support the atmospheric science studies. C.C., M.G., M.B. and V.A. analysed InSight imaging and wind data to support aeolian science studies. C.L.J., A. Mittelholz and C.T.R. analysed InSight magnetometer data to support studies of the atmosphere-induced magnetic signatures. L.M.-S., S.N., J.T., A. Lepinette, A. Molina., M.M.-J., J.G.-E., V.P. and J.-A.R.-M. produced the wind and temperature data from TWINS raw measurements and provided guidance on interpreting these measurements. B.T.C. and S.S. built the Mars Weather Service interface used by the team to explore the InSight meteorological data. W.B.B. and S.E.S. lead the InSight mission and helped to place this study in the broader context of the whole InSight mission. All authors contributed to the investigations, manipulated part of the InSight data reported in this paper and provided comments in the process of writing this paper.

Competing interests

The authors declare no competing interests.

Additional information

Extended data is available for this paper at https://doi.org/10.1038/s41561-020-0534-0.

Correspondence and requests for materials should be addressed to D.B. or A.S.

Peer review information Primary Handling Editor: Stefan Lachowycz.

Reprints and permissions information is available at www.nature.com/reprints.

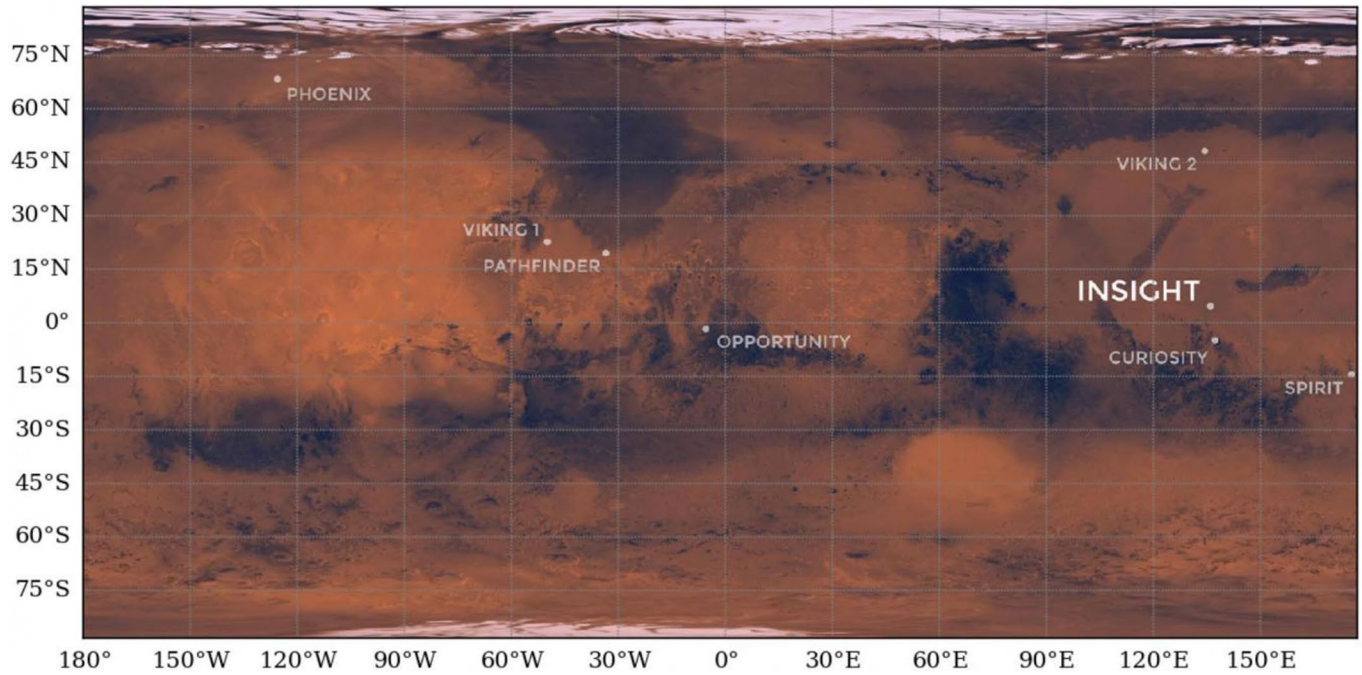

Extended Data Fig. 1 | Location of the InSight landing site on Mars, along with other landers and rovers having operated at the surface of Mars. PIA22232 with added longitude/latitude coordinates.

InSight sols	0	8	32	57	85	113	143	174	207
Solar longitude L_s (°)	295	300	315	330	345	0	15	30	45

Extended Data Fig. 2 | Correspondence between InSight sols and solar longitude Ls for the first 200 sols of the InSight mission. Further details on solar longitude are provided in the *Methods* Section.

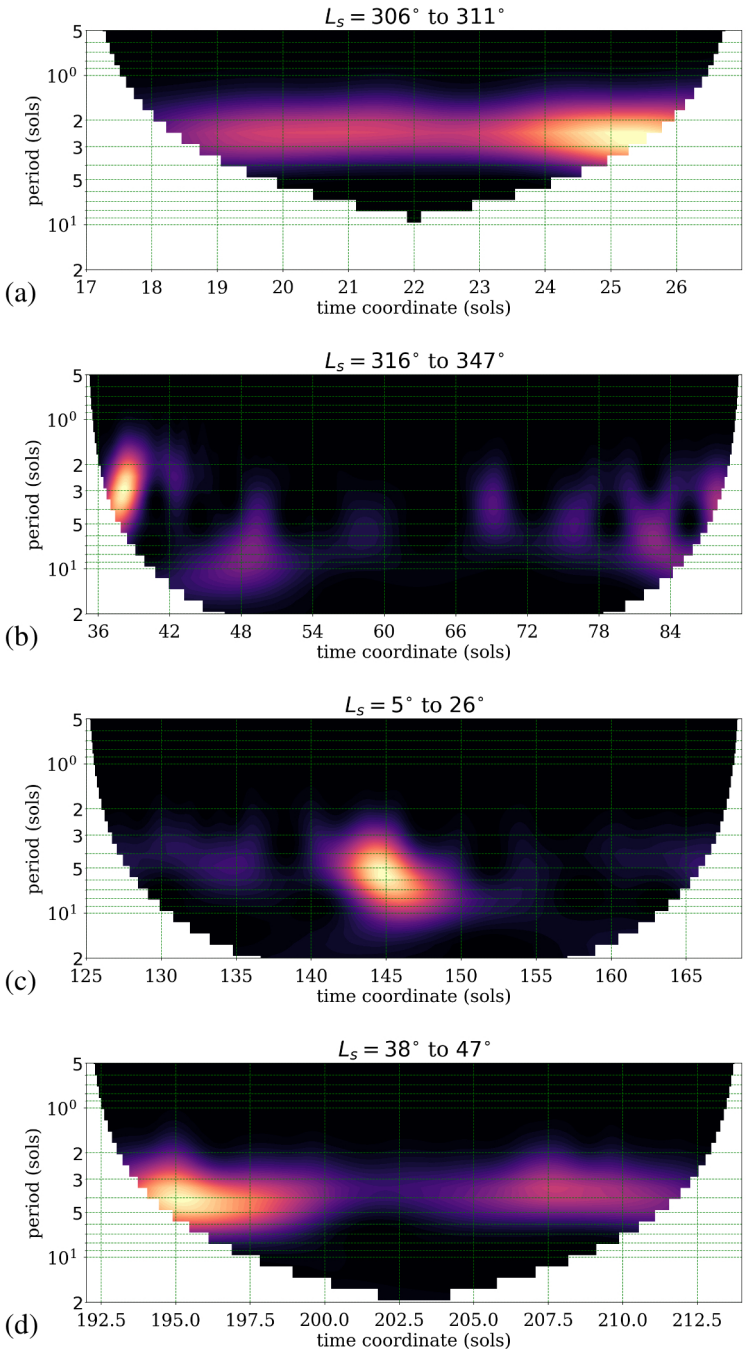

Extended Data Fig. 3 | Wavelet analysis of excerpts of the pressure signal in Figure 3a. Analysis is shown for northern winter (a), regional dust storm conditions (b), and northern spring (c,d). Colors show power spectra (brighter colors for higher power spectra, x-axes show the InSight sol, y-axes show detected periods). Power spectra are only shown inside the cone of influence.

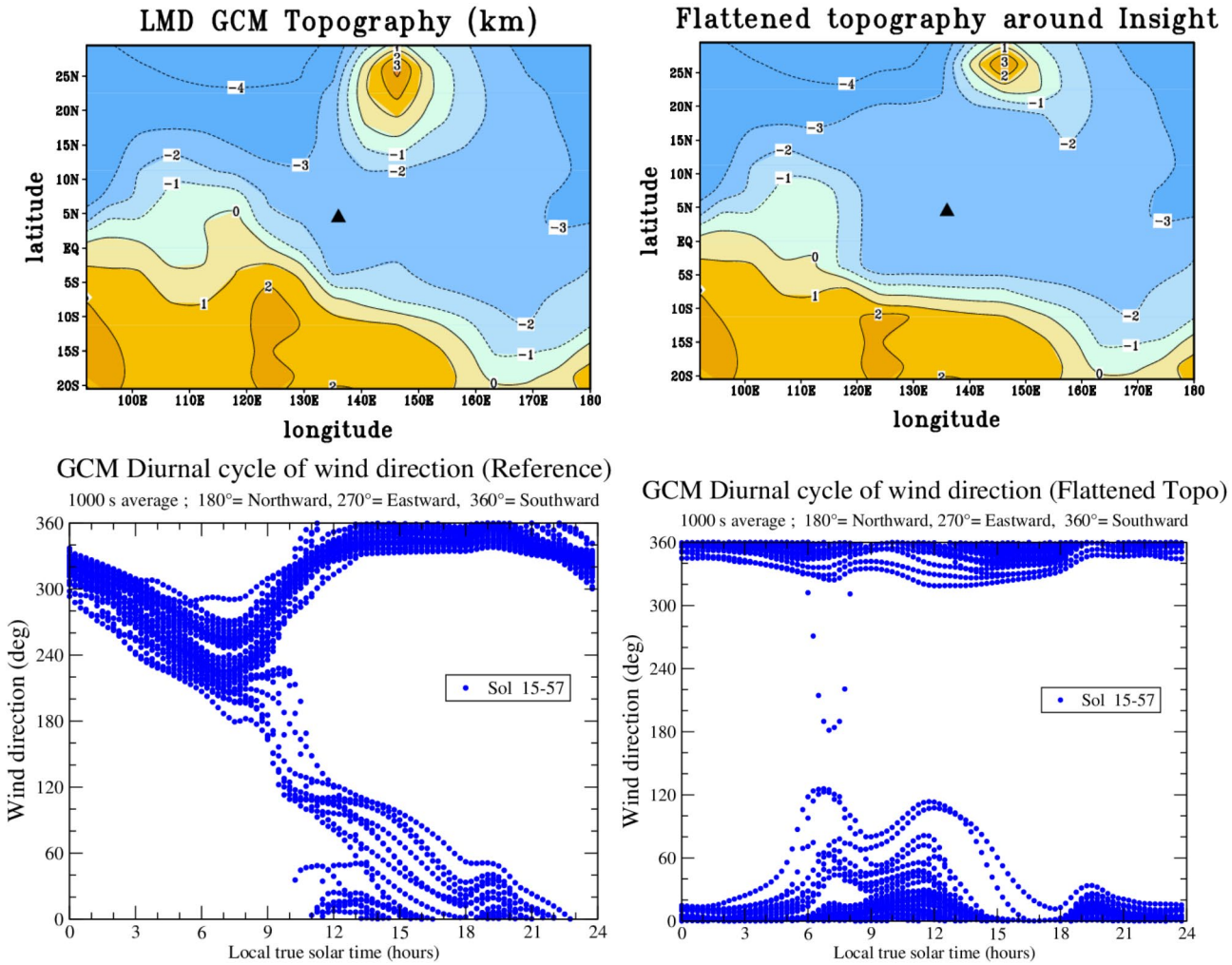

Extended Data Fig. 4 | Atmospheric flows related to the moderate regional slope surrounding the InSight landing site account for the diurnal variability in wind direction. The left panels show the topography and the simulated diurnal cycle of wind direction in the global climate model referenced in the pre-landing study[7]. The right panels show the exact same simulation with flattened topography set as indicated in the top right plot. The thermal tides signal (e.g. in the diurnal cycle of atmospheric pressure) is similar in the two simulations.

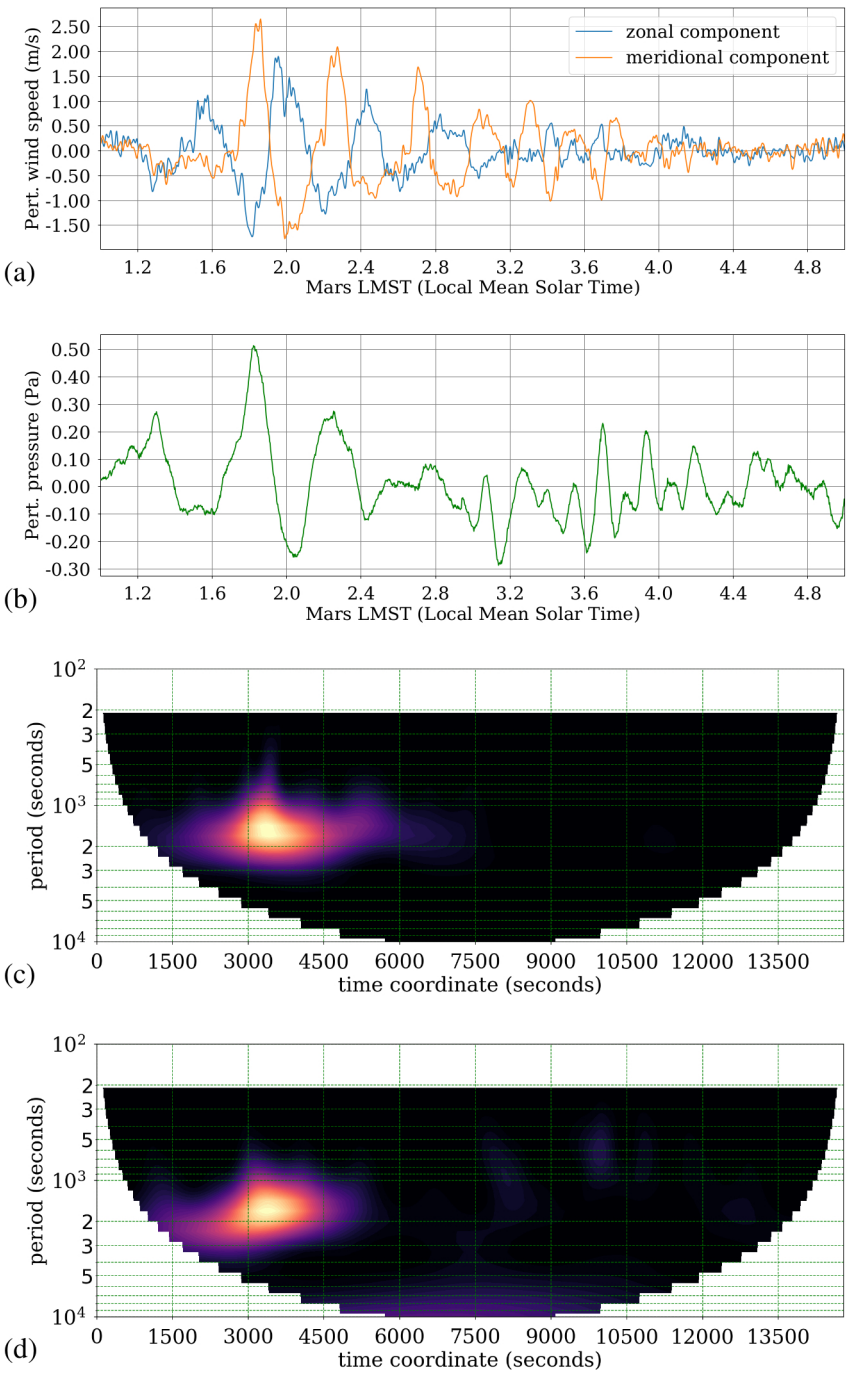

Extended Data Fig. 5 | Nighttime atmospheric measurements by InSight on sol 142, showing simultaneous gravity-wave oscillations of pressure and winds. (a) Perturbations of the zonal and meridional wind components, obtained by first removing high-frequency fluctuations from raw wind measurements using a 100-s smoothing window, then subtracting the long-term variations obtained by a 3700-s (one martian-hour) smoothing window. (b) Perturbations of pressure obtained similarly as (a), except 100-s low-pass filtering is not performed. (c) Wavelet analysis of the perturbation zonal component shown in (a), with similar range on the x-axis as in (a). (d) Same as (c) for the perturbation pressure shown in (b).

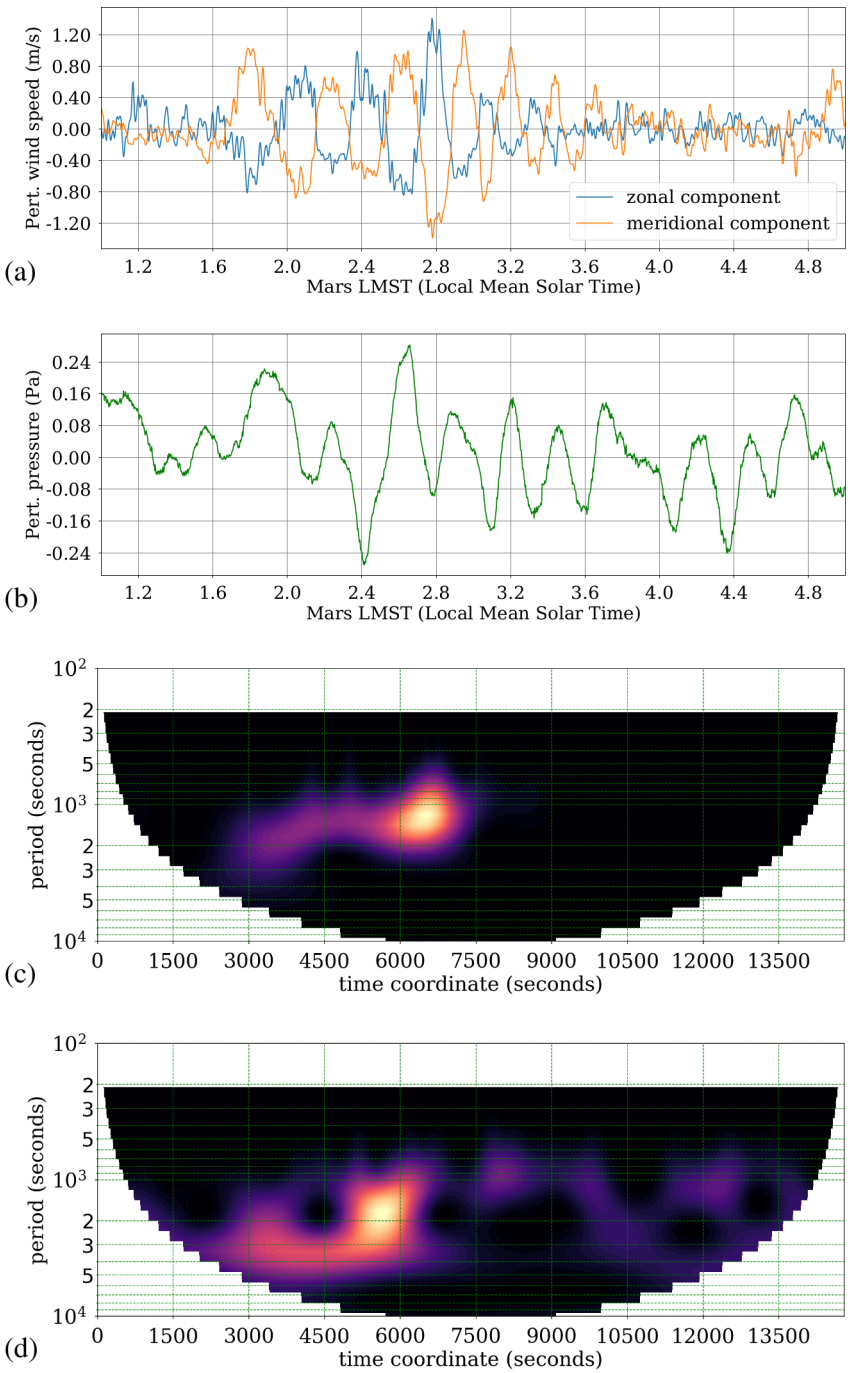

Extended Data Fig. 6 | Nighttime atmospheric measurements by InSight on sol 150, showing simultaneous gravity-wave oscillations of pressure and winds. Figures follow the same principles and organization as Extended Data Fig. 5.

DROP	LTST	SOL
-9.18	13.53	065
-5.76	14.13	019
-5.67	12.73	039
-5.18	14.16	170
-4.91	11.34	191
-4.82	13.71	019
-4.08	12.83	166
-4.05	11.99	065
-4.00	13.78	026
-3.84	12.74	026
-3.80	14.10	178
-3.76	14.21	211
-3.75	12.24	024
-3.71	9.40	170
-3.69	11.11	148

Extended Data Fig. 7 | The 15 strongest vortex induced pressure drops detected by InSight in the first 220 sols of operations. The values of pressure drops in this table, as well as in Figures 5a and 5b, are obtained after removing from pressure measurements the low-frequency pressure variations obtained by applying a 1000-s smoothing window.

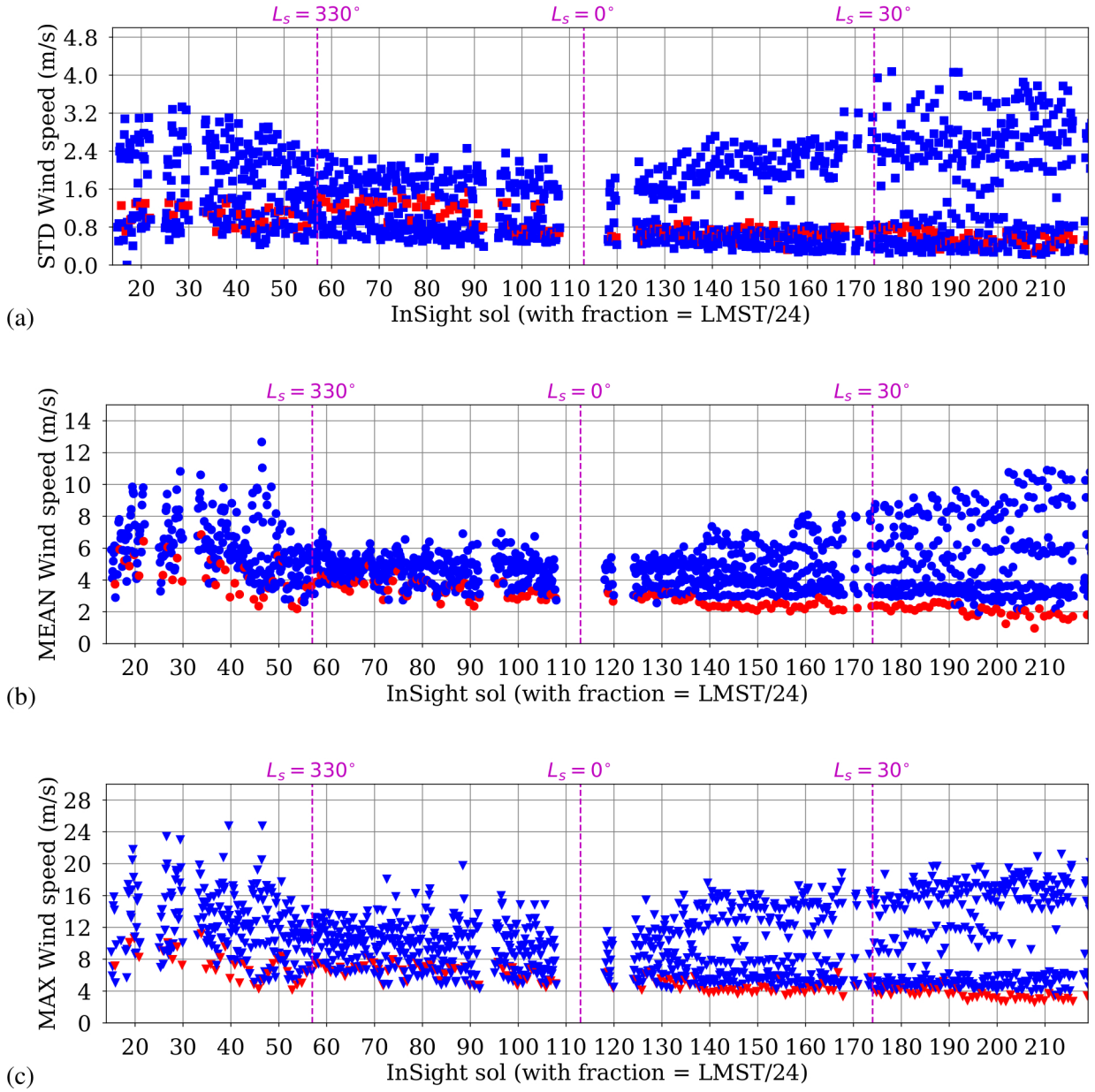

Extended Data Fig. 8 | InSight wind speed measurements shown for the first 220 sols of operations (only sols with complete wind measurements are included in this figure). In each 3-hour bin, (a) standard deviation, (b) average wind speed, and (c) maximum wind speed are displayed. The red dots denote the points corresponding to the bin in the interval 18-21 hours LMST, which is the evening 'quiet' regime described in the main text.